PAPER • OPEN ACCESS

Density-functional-theory approach to the Hamiltonian adaptive resolution simulation method

View the article online for updates and enhancements.

Density-functional-theory approach to the Hamiltonian adaptive resolution simulation method

L A Baptista[1] , **R C Dutta**[1] , **M Sevilla**[1] , **M Heidari**[1] , **R Potestio**[2,3] ,
K Kremer[1] **and R Cortes-Huerto**[1,*]

[1] Max Planck Institute for Polymer Research, Ackermannweg 10, 55128, Mainz, Germany
[2] Physics Department, University of Trento, via Sommarive, 14 I-38123 Trento, Italy
[3] INFN-TIFPA, Trento Institute for Fundamental Physics and Applications, I-38123 Trento, Italy

E-mail: corteshu@mpip-mainz.mpg.de

CrossMark

Abstract

In the Hamiltonian adaptive resolution simulation method (H–AdResS) it is possible to simulate coexisting atomistic (AT) and ideal gas representations of a physical system that belong to different subdomains within the simulation box. The Hamiltonian includes a field that bridges both models by smoothly switching on (off) the intermolecular potential as particles enter (leave) the AT region. In practice, external one-body forces are calculated and applied to enforce a reference density throughout the simulation box, and the resulting external potential adds up to the Hamiltonian. This procedure suggests an apparent dependence of the final Hamiltonian on the system's thermodynamic state that challenges the method's statistical mechanics consistency. In this paper, we explicitly include an external potential that depends on the switching function. Hence, we build a grand canonical potential for this inhomogeneous system to find the equivalence between H–AdResS and density functional theory (DFT). We thus verify that the external potential inducing a constant density profile is equal to the system's excess chemical potential. Given DFT's one-to-one correspondence between external potential and equilibrium density, we find that a Hamiltonian description of the system is compatible with the numerical implementation based on enforcing the reference density across the simulation box. In the second part of the manuscript, we focus on assessing our approach's convergence and computing efficiency concerning various model parameters, including sample size and solute concentrations. To this aim, we compute the excess chemical potential of water, aqueous urea solutions and Lennard–Jones (LJ) mixtures. The results' convergence and accuracy are convincing in all cases, thus emphasising the method's robustness and capabilities.

(Some figures may appear in colour only in the online journal)

---

1. Introduction

In the adaptive resolution method [1–5] (AdResS) and its Hamiltonian variant (H–AdResS) [6, 7] it is possible to simulate atomistic (AT) and ideal gas representations of a physical system coexisting within the simulation box [8, 9]. A hybrid (HY) region connects both representations via a field that switches on (off) intermolecular interactions as molecules enter (leave) the AT region (figure 1). External one-body forces are computed and applied to ensure a constant density profile, and once integrated, the corresponding potential energy adds up to the Hamiltonian. This external potential has been identified with the excess chemical potential between the regions of the system [6, 7, 9]. Nevertheless, this technical procedure raises the question of whether the modified Hamiltonian becomes dependent upon the specific thermodynamic state. In consequence, such a dependence would question the use of the H–AdResS Hamiltonian in the context of classical statistical mechanics.

In this paper, we use the statistical mechanics formalism of H–AdResS, developed by Español and collaborators [10], where the external potential directly enters the Hamiltonian as a functional of the switching field. We use this Hamiltonian to build a grand canonical potential that, for such an inhomogeneous system, is a functional of the external potential [11]. Since the subsystem of interest is in contact with an ideal gas, sampling the grand canonical potential does not involve any major difficulty, as we have recently demonstrated [12]. As a matter of fact, the adaptive resolution framework has been established as a method to perform simulations in the grand canonical ensemble [12–18]. With this grand potential [19, 20], we find an equivalent classical density functional theory (DFT) approach to H–AdResS. Once the equivalence between DFT and H–AdResS is established, we show that the external potential that enforces the reference, ideal gas, density throughout the system is precisely the excess chemical potential. Given DFT's one-to-one correspondence between the density and the external potential, we validate the standard H–AdResS strategy based on enforcing a uniform density profile to compute the Hamiltonian's external potential and, therefore, the excess (over the ideal gas) chemical potential [9]. The calculation of excess chemical potentials within the H–AdResS formalism closely resembles the thermodynamic integration method [21]. For such a reason we have called it spatially-resolved thermodynamic integration (SPARTIAN) [9].

In the second part of the paper, we test the current numerical implementation of the SPARTIAN method [9]. In particular, we compute the excess chemical potential of pure water, aqueous urea solutions and LJ mixtures. Additionally to the comparison with chemical potential values reported in the literature, when available, we tested the convergence of the results with model parameters such as size of the HY region, system size and composition. Our results confirm the method's robustness and efficiency and establish it as an alternative approach to compute free energy differences. We also assess the method's computing efficiency concerning fully AT simulations. These results highlight the necessity to either fine-tune the domain decomposition conditions in the ideal gas region or to reduce its size to a minimum and use our recently developed particle-insertion method [12] to include an infinite reservoir effectively.

The paper is organised as follows: in section 2, we present the H–AdResS method in terms of DFT. In section 3, we report the calculations of the test systems' excess chemical potential. Finally, we discuss our results and conclude in section 4.

2. H–AdResS as an inhomogeneous system: connection to DFT

We write the adaptive resolution Hamiltonian [6, 7, 9] for a molecular fluid composed of N_a atoms, distributed among N molecules, as

$$H_{[\lambda]}(r,p) = \mathcal{K} + V^{\text{intra}} + \sum_{\alpha=1}^{N} \{\lambda_\alpha V_\alpha + V^{\text{ext}}(\lambda_\alpha)\}, \quad (1)$$

with (r,p) positions and momenta and $\mathcal{K} = \sum_{i=1}^{N_a} \mathbf{p}_i^2/2m_i$ is the total kinetic energy of the system. Latin indices run over atoms and greek indices over molecules. The term $V^{\text{intra}} = \sum_{\alpha=1}^{N} \sum_{i \neq j \in \alpha} V^{\text{intra}}(r_{ij})$ accounts for intra-molecular interactions, with r_{ij} the separation between atoms i and j belonging to the same molecule α. The intermolecular interactions are included in the term $V_\alpha = \frac{1}{2} \sum_{\beta \neq \alpha} \sum_{i \neq j} V(|\mathbf{r}_{\alpha i} - \mathbf{r}_{\beta j}|)$ with $\mathbf{r}_{\alpha i}$ the position of the atom i in molecule α. The switching field determines the molecules' identity, with $\lambda_\alpha \equiv \lambda(\mathbf{R}_\alpha)$ and $\mathbf{R}_\alpha$ the position of the centre of mass of the molecule α. When $\lambda = 0$ the Hamiltonian describes an homogeneous ideal gas system provided $V^{\text{ext}}(0) = $ constant. In particular, we set $V^{\text{ext}}(0) = 0$. For $0 < \lambda \leqslant 1$, the Hamiltonian describes an inhomogeneous system, namely, an interacting system in the presence of an external field (figure 1). We assume that the system (AT and ideal gas representations) is embedded in a reservoir of infinite size at temperature T and chemical potential μ^{id}, the chemical potential of the ideal gas (IG). In practice, by using the Hamiltonian in equation (1), we have recently demonstrated that the numerical implementation of these conditions is straightforward [12]. Here, we calculate the grand canonical partition function corresponding to the adaptive resolution Hamiltonian (1)

$$\mathcal{Z}[\lambda] = \text{Tr}\{\exp(-\beta(H_{[\lambda]} - \mu(\lambda)N))\}, \quad (2)$$

with $\beta = 1/k_{\text{B}}T$ and k_{B} being the Boltzmann's constant. We use the classical trace notation [19, 20] to avoid writing explicitly the integral over all particle momenta and positions and the sum over all possible system sizes

$$\text{Tr} = \sum_{N_a=0}^{\infty} \frac{1}{h^{3N_a} N_a!} \int d^{3N_a} r \int d^{3N_a} p,$$

with h the Planck's constant.

By using the partition function (2), we define the equilibrium distribution function as [19, 20]

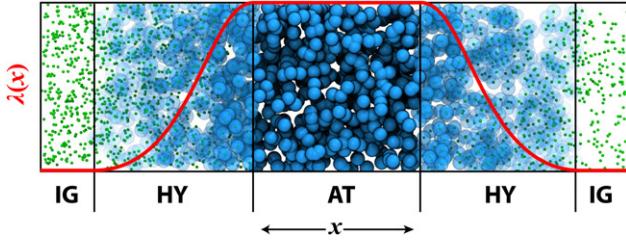$$f_0[\lambda] = \frac{1}{\mathcal{Z}[\lambda]} \exp(-\beta(H_{[\lambda]} - \mu(\lambda)N), \quad (3)$$

Figure 1. Schematic representation of a typical adaptive resolution slab. The central, fully AT, region is embedded into a reservoir of IG particles. An interfacial, HY, region connects AT and IG subsystems via a switching field λ that smoothly switches on (off) intermolecular interactions as molecules leave (enter) the IG region. An external field, not shown, counterbalances free energy barriers such that molecules freely diffuse between regions.

which satisfies that $\text{Tr} f_0[\lambda] = 1$. The thermal average of an operator $\hat{O}$ is given by $\langle \hat{O} \rangle^{[\lambda]} = \text{Tr}\{f_0[\lambda]\hat{O}\}$. In particular, the external potential makes the system's density inhomogeneous. We use the previous definition of thermal average to write the equilibrium density profile in the form

$$\rho_0^{[\lambda]}(\mathbf{r}) = \langle \hat{\rho}(\mathbf{r}) \rangle^{[\lambda]}, \tag{4}$$

with $\hat{\rho}(\mathbf{r}) = \sum_\alpha \delta(\mathbf{R}_\alpha - \mathbf{r})$.

Using an arbitrary distribution function $f[\lambda]$, that satisfies the condition $\text{Tr} f[\lambda] = 1$, Mermin, in the context of the inhomogeneous electron gas, proposed a functional form for the grand potential [22] that we write for our particular case as

$$\Omega_{[\lambda]}[f[\lambda]] = \text{Tr}\{f[\lambda](H_{[\lambda]} - \mu(\lambda)N + \beta^{-1}\ln f[\lambda])\}. \tag{5}$$

By replacing the equilibrium distribution, we obtain

$$\Omega_{[\lambda]}[f_0[\lambda]] = -\beta^{-1}\ln \mathcal{Z}[\lambda] = \Omega_{[\lambda]}^0 \tag{6}$$

the definition of grand potential in terms of the grand canonical partition function.

Using the density operator $\hat{\rho}$, we can rewrite the external potential as

$$\sum_\alpha^N V^{\text{ext}}(\lambda_\alpha) = \int d\mathbf{r} \sum_{\alpha=1}^N \delta(\mathbf{R}_\alpha - \mathbf{r})V^{\text{ext}}(\lambda(\mathbf{r}))$$

$$= \int d\mathbf{r}\, \hat{\rho}(\mathbf{r})V^{\text{ext}}(\lambda(\mathbf{r})). \tag{7}$$

The density distribution $f[\lambda]$ is, in general, a functional of the density $\rho^{[\lambda]}(\mathbf{r})$. Therefore [11, 19, 20], by using the Hamiltonian (1) we write the grand potential as a functional of the density

$$\Omega_{[\lambda]}[\rho^{[\lambda]}(\mathbf{r})] = \text{Tr}\{f[\lambda](H_{[\lambda]} - \mu(\lambda)N + \beta^{-1}\ln f[\lambda])\}$$

$$= \text{Tr}\left\{f[\lambda]\left(\mathcal{K} + V^{\text{int}} + \sum_{\alpha=1}^N \lambda_\alpha V_\alpha\right.\right.$$

$$\left.\left. + \beta^{-1}\ln f[\lambda] + \sum_{\alpha=1}^N V^{\text{ext}}(\lambda_\alpha) - \mu(\lambda)N\right)\right\}$$

$$= F_{[\lambda]}[\rho^{[\lambda]}(\mathbf{r})] + \int d\mathbf{r}\, \rho^{[\lambda]}(\mathbf{r})$$

$$\times (V^{\text{ext}}(\lambda(\mathbf{r})) - \mu(\lambda(\mathbf{r}))), \tag{8}$$

in which we make use of equation (7) where the total external potential is written as a functional of the density. The functional $F_{[\lambda]}[\rho^{[\lambda]}]$ is the intrinsic Helmholtz free energy corresponding to the Hamiltonian (1), which is independent of the external potential:

$$F_{[\lambda]}[\rho^{[\lambda]}] = \text{Tr}\left\{f[\lambda]\left(\mathcal{K} + V^{\text{int}} + \sum_{\alpha=1}^N \lambda_\alpha V_\alpha + \beta^{-1}\ln f[\lambda]\right)\right\}. \tag{9}$$

The last two equations provide us with a direct connection between H–AdResS and DFT. The expression (8) is a functional Legendre transform relating the Helmholtz free energy and the grand potential [11].

To understand equation (8), we underline that the system is inhomogeneous, and the grand potential is a functional of the external potential [11, 20]. That is

$$\frac{\delta\Omega_{[\lambda]}}{\delta(\mu(\lambda(\mathbf{r})) - V^{\text{ext}}(\lambda(\mathbf{r})))} = -\rho^{[\lambda]}(\mathbf{r}), \tag{10}$$

which is consistent with the thermodynamic identity $\partial\Omega/\partial\mu = -N$.

Written as a functional of the density, $\Omega_{[\lambda]}[\rho^{[\lambda]}(\mathbf{r})]$ represents the cost in free energy necessary to find the system at precisely the density $\rho^{[\lambda]}(\mathbf{r})$ [11]. In particular, we find the density field, $\rho_0^{[\lambda]}(\mathbf{r})$, that minimises this cost by evaluating the functional derivative of the grand potential with respect to the density. Hence, the grand potential satisfies

$$\left.\frac{\delta\Omega_{[\lambda]}[\rho^{[\lambda]}]}{\delta\rho^{[\lambda]}}\right|_{\rho^{[\lambda]}=\rho_0^{[\lambda]}} = 0, \tag{11}$$

thus implying

$$\left.\frac{\delta F_{[\lambda]}[\rho^{[\lambda]}]}{\delta\rho^{[\lambda]}}\right|_{\rho^{[\lambda]}=\rho_0^{[\lambda]}} = -V^{\text{ext}}(\lambda(\mathbf{r})) + \mu(\lambda(\mathbf{r})). \tag{12}$$

The exact form of the intrinsic free energy functional $F_{[\lambda]}[\rho^{[\lambda]}]$ is, in general, unknown. However, we can re-write it as

$$F_{[\lambda]}[\rho^{[\lambda]}] = F_{[\lambda]}^{\text{exc}}[\rho^{[\lambda]}] + F_{[0]}[\rho^{[0]}], \tag{13}$$

with $F_{[\lambda]}^{\text{exc}}[\rho^{[\lambda]}]$ the excess free energy, calculated with respect to the free energy of the reference system (ideal gas), $F_{[0]}[\rho^{[0]}]$. To ensure thermodynamic consistency in the adaptive resolution description, we require the free energy being independent of λ [10]. Nevertheless, we anticipate here that this condition could be changed to induce non-equilibrium conditions in the system [12]. In equilibrium, $F_{[\lambda]}^{\text{exc}}[\rho^{[\lambda]}] = 0$, thus,

$$F_{[0]}[\rho^{[0]}(\mathbf{r})] = F^{\text{id}}[\rho(\mathbf{r})] = \beta^{-1}\int d\mathbf{r}\rho(\mathbf{r})\{\ln(\lambda_T^3\rho(\mathbf{r})) - 1\}, \tag{14}$$

with F^{id} the Helmholtz free energy of the IG (our reference state at $\lambda = 0$), $\rho^{[0]}(\mathbf{r}) = \rho(\mathbf{r})$ and $\lambda_T = (\hbar^2\beta/2\pi m)^{1/2}$ the

thermal, de Broglie, wavelength. We rewrite equation (12) as

$$\frac{\delta F^{\text{id}}[\rho(\mathbf{r})]}{\delta \rho(\mathbf{r})} = -V^{\text{ext}}(\lambda(\mathbf{r})) + \mu^{\text{exc}}(\lambda(\mathbf{r})) + \mu^{\text{id}}, \qquad (15)$$

with $\mu^{\text{exc}}(\lambda(\mathbf{r})) = \mu(\lambda(\mathbf{r})) - \mu^{\text{id}}$, a continuous function of λ, $\mu^{\text{id}} = \beta^{-1} \ln(\lambda_{\text{dB}}^3 \rho_0)$ and ρ_0 the reference (IG) density. By replacing μ^{id} into the previous equation, we find

$$\rho(\mathbf{r}) = \rho_0 \exp(-\beta\{V^{\text{ext}}(\lambda(\mathbf{r})) - \mu^{\text{exc}}(\lambda(\mathbf{r}))\}), \qquad (16)$$

where it is apparent that this density field does not explicitly depend on the switching field. Indeed, this expression shows that the external potential determines the density. In particular, the condition

$$V^{\text{ext}}(\lambda(\mathbf{r})) = \mu^{\text{exc}}(\lambda(\mathbf{r})) \qquad (17)$$

guarantees a constant density ρ_0. In other words, the external potential that enforces the reference density for the whole system is equal to the excess chemical potential.

This result provides an interesting parallel with DFT. In the latter, we apply an external potential and then use a self-consistent approach to find the corresponding system's equilibrium density. By considering the one-to-one correspondence between external potential and equilibrium density as provided by DFT, the approach generally used in H–AdResS naturally follows. We enforce a uniform density throughout the simulation box and then calculate the resulting external potential $V^{\text{ext}}(\lambda(\mathbf{r}))$. This is particularly useful to compute chemical potentials of molecular fluids and liquid mixtures, since $V^{\text{ext}}(1) = \mu^{\text{exc}}$ with μ^{exc} the excess chemical potential of the AT system over the ideal gas.

To use the Hamiltonian (1) to perform molecular dynamics simulations, we need to compute the forces. The force, calculated as minus the gradient of the Hamiltonian, acting on a molecule α is given by:

$$\mathbf{F}_\alpha = \mathbf{F}_\alpha^{\text{int}} + \sum_{\beta \neq \alpha} \left\{ \frac{\lambda_\alpha + \lambda_\beta}{2} \mathbf{F}_{\alpha|\beta} \right\}$$
$$- \nabla_\alpha \lambda_\alpha \left[V_\alpha + V^{'\text{ext}}(\lambda) \Big|_{\lambda=\lambda_\alpha} \right], \qquad (18)$$

with $\mathbf{F}_\alpha^{\text{int}}$ and $\mathbf{F}_{\alpha|\beta}$ the forces due to the intra- and intermolecular potentials, respectively, and $V^{'\text{ext}} = \text{d}V^{\text{ext}}/\text{d}\lambda$. The force proportional to the gradient of the switching field weakly violates Newton's third law and momentum conservation, and introduces spurious density and pressure inhomogeneities into the system. Since we do not know *a priori* the external potential, we cannot directly compute its derivative with respect to λ. However, we can obtain a first approximation to $V^{'\text{ext}}(\lambda)$ by taking a closer look at the invariance of the Helmholtz free energy with respect to the switching field [10]

$$\frac{\delta F_{[\lambda]}(\rho(\mathbf{r}))}{\delta \lambda(\mathbf{r})} = \frac{\delta \Omega_{[\lambda]}(\rho(\mathbf{r}))}{\delta \lambda(\mathbf{r})} - \frac{\delta}{\delta \lambda(\mathbf{r})}$$
$$\times \int \text{d}\mathbf{r}\, \rho(\mathbf{r}) (V^{\text{ext}}(\lambda(\mathbf{r})) - \mu(\lambda(\mathbf{r}))) = 0, \quad (19)$$

where we use the inverse of equation (8) for the density field $\rho(\mathbf{r})$. Following the condition given by equation (17), the

functional derivative of the integral vanishes. Using equation (6), we find

$$\frac{\delta \Omega_{[\lambda]}(\rho(\mathbf{r}))}{\delta \lambda(\mathbf{r})} = \text{Tr}\left\{ f[\lambda] \frac{\delta H_{[\lambda]}}{\delta \lambda(\mathbf{r})} \right\}$$
$$- \text{Tr}\left\{ N \frac{\exp(-\beta H_{[\lambda]})}{\mathcal{Z}[\lambda]} \frac{\delta z[\lambda]}{\delta \lambda(\mathbf{r})} \right\} = 0, \quad (20)$$

with $z[\lambda] = \exp(\beta\mu(\lambda))$ the system's fugacity. In general, the two terms on the rhs of the previous equation cancel each other out to guarantee a uniform density profile. There is also the possibility that every term remains invariant with respect to changes in $\lambda(\mathbf{r})$. In particular, if the fugacity of the system does not depend on λ, then the pressure, and not the density, is constant throughout the simulation box [10]. This assumption implies that

$$\text{Tr}\left\{ f[\lambda] \frac{\delta H_{[\lambda]}}{\delta \lambda(\mathbf{r})} \right\} = \text{Tr}\left\{ f[\lambda] \sum_{\alpha=1}^{N} (V_\alpha + V^{'\text{ext}}(\lambda(\mathbf{r}))) \delta(\mathbf{R}_\alpha - \mathbf{r}) \right\}$$
$$= \left\langle \sum_{\alpha=1}^{N} V_\alpha \delta(\mathbf{R}_\alpha - \mathbf{r}) \right\rangle^{[\lambda]}$$
$$+ V^{'\text{ext}}(\lambda(\mathbf{r})) \rho^{[\lambda]}(\mathbf{r}) = 0, \qquad (21)$$

which allows us to evaluate $V^{'\text{ext}}$ in terms of thermal averages over quantities that we know. From a practical viewpoint, we use the local equilibrium approximation discussed in reference [10]. When λ is sufficiently smooth, the thermal average is approximated to an average computed at a constant value of the switching field at a given position $\mathbf{r}$. That is, $\langle \cdots \rangle^{[\lambda]} \approx \langle \cdots \rangle^\lambda$ [10]. By integrating over space we obtain,

$$\langle V \rangle^\lambda + V^{'\text{ext}}(\lambda)N = 0, \qquad (22)$$

with $V = \sum_\alpha V_\alpha$. Finally, we obtain [6]

$$V^{'\text{ext}}(\lambda)|_{\lambda=\lambda_\alpha} = -\langle V \rangle^{\lambda=\lambda_\alpha}/N \approx -\langle V \rangle_{\mathbf{R}_\alpha}. \qquad (23)$$

By inserting this *drift* term in the force (18) we see that, on average, the term proportional to the gradient of λ vanishes. Therefore, we obtain a description of the system that on average satisfies Newton's third law and linear momentum conservation. This is an important issue because significant artefacts are introduced in the simulation if these conditions are not fulfiled [23]. Furthermore, by using this force, we are implicitly ensuring a constant pressure throughout the simulation box [6, 10].

We now return to adaptive resolution setups at constant density. To enforce this condition, we compute and apply, iteratively, an external force, dubbed *thermodynamic force* [14, 24], given by

$$\mathbf{F}_{n+1}^{\text{th}} = \mathbf{F}_n^{\text{th}} + \frac{c \nabla \rho(x)_n}{\rho_0}, \qquad (24)$$

with c a parameter with units of energy. $\nabla \rho(x)_n$ is the gradient of the density profile computed at the nth step of the iteration. The computation of this force converges when $\nabla \rho = 0$, that is, when the density becomes ρ_0 everywhere.

Hence, we have that the total external force acting on a molecule α, instantaneously present in the HY region, becomes

$$-\nabla_{\mathbf{R}_\alpha} V^{\text{ext}}(\lambda)|_{\lambda=\lambda_\alpha} = \langle V \rangle_{\mathbf{R}_\alpha} \nabla \lambda(\mathbf{R}_\alpha) + \mathbf{F}_\alpha^{\text{th}}. \qquad (25)$$

The integral over space of this force will give us the external potential that, in virtue of equation (17), equates the excess chemical potential, provided the density is constant and equal to ρ_0 throughout the simulation box. Due to the similitude between this approach and Kirkwood's thermodynamic integration (KTI) [21], in the following sections, we refer to this method to compute free energy differences as the spatially-resolved thermodynamic integration (SPARTIAN) method [9]. The comparison with KTI also implies that to compute μ^{exc} it is sufficient to enforce the target density at the AT and IG regions, which corresponds to the selection of a different thermodynamic path to compute the integral.

We conclude this section highlighting that the generalisation of this procedure to the study of mixtures is straightforward [7, 19]. In the following section, we will provide a few examples where excess chemical potentials of complex liquids and liquid mixtures are computed and compared with results available in the literature.

3. Simulation results

In this section, we present the calculation of the excess chemical potential for SPC/E [25–27] water, LJ mixtures and aqueous urea solutions [28–30]. The aim is to investigate convergence and performance of the calculation using various simulation setups.

3.1. Preliminaries

We use the LAMMPS [31] implementation of SPARTIAN described in references [9, 24]. Namely, we discretise the HY region in bins of size $\delta\lambda$ and δr. To compute the forces, we use the iterative procedure described in reference [24]. We sample each term on the rhs of equation (25) separately, using independent time-intervals. At the end of every interval, the code generates two files containing $\langle V(\lambda) \rangle$ and $\mathbf{F}^{\text{th}}(r)$. As anticipated in the previous section, the analysis of a liquid mixture only requires to compute the corresponding forces acting on every individual component. Thus, in the case of a spherical AT region, with radius r_{AT} and thickness of the HY region d_{HY}, the excess chemical potential for the i-component is calculated as

$$\mu_i^{\text{exc}} = \int_0^1 \mathrm{d}\lambda \, \langle V_i(\lambda) \rangle + \int_{r_{\text{AT}}}^{r_{\text{AT}}+d_{\text{HY}}} \mathrm{d}r \, \mathbf{F}_i^{\text{th}}(r) \cdot \hat{n}, \qquad (26)$$

with $\hat{n}$ a unit vector pointing away from the AT region. The switching function is defined as

$$\lambda(r) = \begin{cases} 1 & r \leqslant r_{\text{AT}} \\ \cos^{14}\left(\dfrac{\pi(r - r_{\text{AT}})}{2d_{\text{HY}}}\right) & r_{\text{AT}} < r \leqslant r_{\text{AT}} + d_{\text{HY}} \\ 0 & r > r_{\text{AT}} + d_{\text{HY}}, \end{cases} \qquad (27)$$
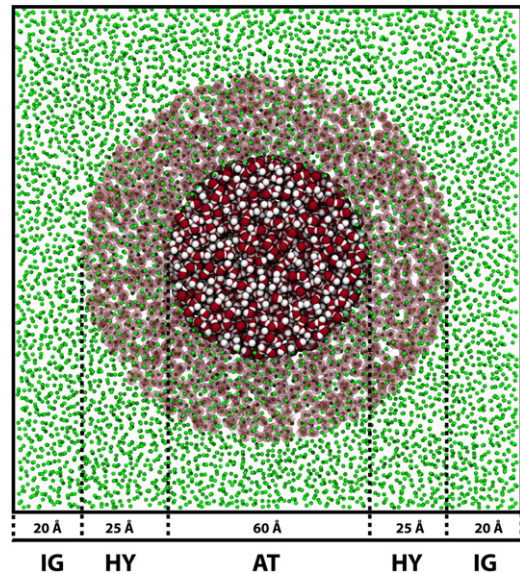

Figure 2. Simulation snapshot showing the SPARTIAN configuration for a pure water calculation. A spherical AT region or radius 30 Å is embedded into a simulation box of linear size of 150 Å. The HY region is a spherical shell of maximum thickness 25 Å, and the IG occupies the remaining free space.

with the exponent 14 selected for numerical convenience [9].

To compute the thermodynamic force (24), we use $c = 1.0$, 0.01 kcal mol^{-1} and 2ϵ to modulate the contribution from $\nabla\rho$ in the case of SPC/E water, aqueous urea solutions and LJ mixtures, respectively. To get a smooth force field, we convolute the density profile with Gaussian functions of width equal to three times the length of a HY region bin. During the simulation, it is possible that two molecules approach each other in the HY region while travelling towards the AT region. Once there, if they get too close to each other, the strong repulsion might create numerical instabilities. To avoid this problem, we introduce a capping radius for all the interactions. The corresponding values are 0.1 σ for LJ mixtures and 0.5 Å for Van der Waals and electrostatic potentials in water and aqueous urea solutions [9].

We use the damped-shifted force potential model (DSF) [32–35] to describe electrostatic interactions. To compare with the results of free energy differences obtained by using Ewald summation, we need to subtract a constant term [9]. In the case of rigid molecules using the SHAKE algorithm [36], this term corresponds to electrostatic intramolecular interactions between i, j atomic pairs, given by $q_i q_j / r_{ij}$ with q_i the charge of the ith atom.

3.2. Size of the HY region

We start with the calculation of $\mu_{\text{WATER}}^{\text{exc}}$ for pure water. We present the simulation setup used in figure 2. We consider a system of 111375 SPC/E [25–27] water molecules in a cubic simulation box, with linear size equal to 150.0 Å. A spherical AT region with radius 30 Å is embedded into a HY region of thickness varying between 10, 15, 20 and 25 Å. The starting point of the calculation corresponds to a fully AT simulation equilibrated for 25 ns at $T = 298.0$ K and $P = 1.0$ bar using
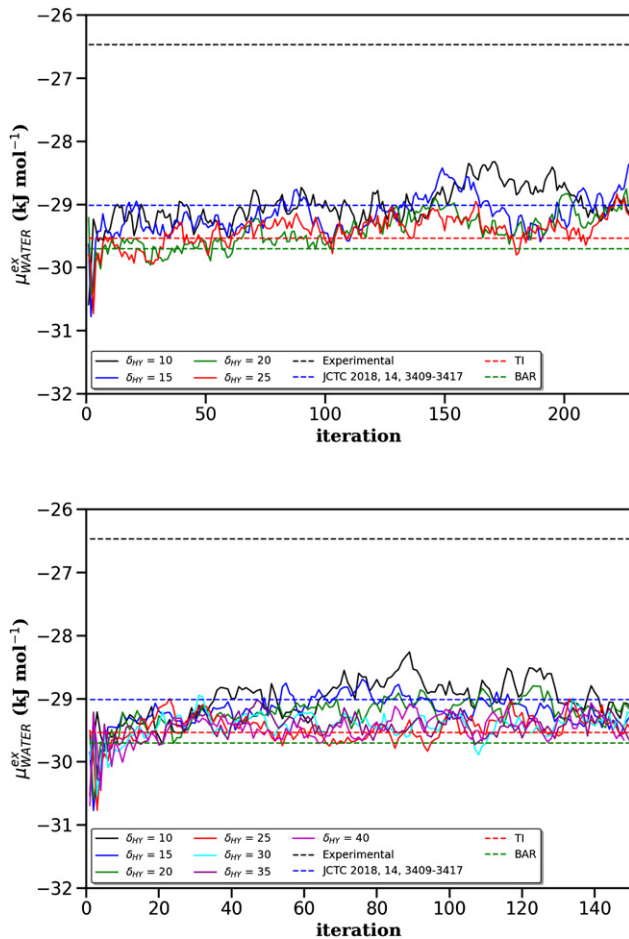
Figure 3. (Top) Excess chemical potential for water obtained for different HY region thicknesses. The linear size of the simulation box is 150 Å. (Bottom) Excess chemical potential for water obtained for different HY region thicknesses. The linear size of the simulation box is 200 Å. In addition to reporting our previous result [9], we compare with the experimental value [37], and with computational results obtained by using TI [38] and the BAR methods [39].

the Nosé–Hoover thermostat and barostat with damping constant equal to 100 fs for both cases. After this step, the systems were equilibrated by 25 ns in the NVT ensemble using Langevin thermostat with damping parameter equal to 100 fs and an integration time step of 1.0 fs.

By starting from the final fully-atomistic configuration, we start the SPARTIAN runs. We simultaneously average both contributions to the force (18) for 20 ps, then at the end of this period, we calculate and apply the forces. This cycle corresponds to a single iteration. After every iteration we use equation (26) to obtain the value of $\mu_{\mathrm{WATER}}^{\mathrm{exc}}$. Results of this procedure, for different sizes of the HY region, are presented in figure 3(top). For reference, we also include the experimental value [37], as well as computational results obtained by using thermodynamic integration (TI) [38] and the Bennett acceptance-ratio (BAR) methods [39].

It is apparent from the figure that the final result is somewhat insensitive to the size of the HY region. With small values of δ_{Hy}, namely 10 and 15 Å, there are larger fluctuations in the result related to poor statistics. Once the sample size

Table 1. Excess chemical potential for water[a]

	μ_{ext} (kJ mol^{-1})	
δ_{HY} (Å)	$L = 150$ Å	$L = 200$ Å
10.0	-28.79 ± 0.18	-28.93 ± 0.13
15.0	-28.91 ± 0.24	-29.31 ± 0.14
20.0	-29.08 ± 0.17	-29.17 ± 0.11
25.0	-29.27 ± 0.21	-29.41 ± 0.16
30.0		-29.36 ± 0.14
35.0		-29.40 ± 0.16
40.0		-29.38 ± 0.17

[a]standard deviation measured over the last twenty iterations.

increases, $\delta_{\mathrm{Hy}} = 20$ and 25 Å, the result convincingly converges after 100 iterations (2 ns) to the value obtained by using the state-of-the-art computational methods considered here.

This picture remains essentially consistent upon increasing the size of the system. Figure 3(bottom) shows similar results for a simulation box of linear size equal to 200 Å. In this case, additionally to the values considered before, we can also investigate the convergence of the result for values of $\delta_{\mathrm{HY}} = 30$, 35 and 40 Å. Similarly to the previous case, the result smoothly converges to the expected $\mu_{\mathrm{WATER}}^{\mathrm{exc}}$ value for the SPC/E model.

The results of this sub-section, averaged over the last twenty iterations, are summarised in table 1.

To conclude this section, we comment on how to choose the size of the HY region. To avoid artefacts arising from finite-size effects, the volume of the AT region should contain the volume defined by the correlation length of the system. Our results indicate that this size constraint also applies to the HY region. Hence, it is advisable to choose the linear size of the HY region larger than the correlation length of the system.

3.3. HPC performance

By using the water system considered in the previous sub-section, we perform a strong scaling analysis. Namely, we select a different number of processors and evaluate the performance of the calculation, measured in units of ns per day. Results are presented in figure 4(top) where it is apparent that fully-atomistic simulations, for both sizes included in this study (blue symbols), exhibit a better scaling than their SPARTIAN counterparts (black and green symbols). This behaviour is due to lack of optimisation in domain decomposition and load balancing in the SPARTIAN implementation. Processors assigned to the IG region run more idle than the ones assigned to the AT and HY regions thus hindering parallel processing and communication.

Upon increasing the size of the system, in both fully-atomistic and SPARTIAN calculations there is a substantial and proportionally similar decrease in computing efficiency. Furthermore, in the case of SPARTIAN calculations, as presented in figure 4(bottom), there is a slight decrease in efficiency upon increasing the size of the HY region while keeping the size of the AT region constant. Indeed, figure 5 illustrates the performance of the SPARTIAN calculation as a function of the HY region thickness, for systems with fixed linear sizes (150 and 200 Å), AT region size, and number of
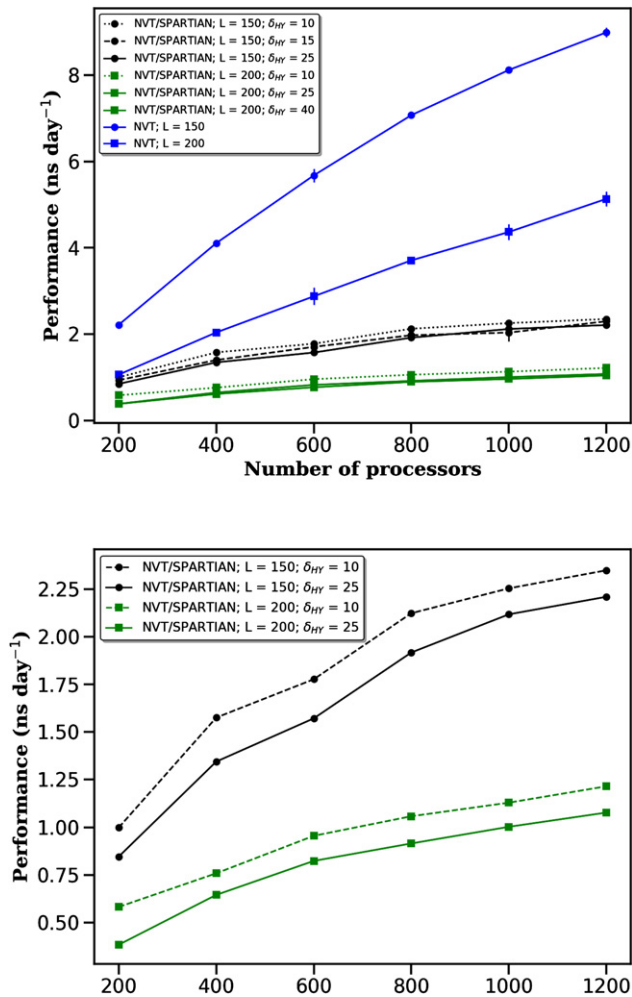
Figure 5. Performance of the SPARTIAN calculation as a function of the HY region thickness. Calculations were performed by using 800 processors.

Figure 4. (Top) Performance of the SPARTIAN and NVT as a function of the number of processors. (Bottom) Performance of the SPARTIAN and NVT as a function of the number of processors for HY region thickness equal to 10.0 Å and 25.0 Å

processors (800). Both tendencies confirm that the rather modest SPARTIAN performance is mainly due to the parallelisation and communication issues mentioned above. The default domain decomposition in LAMMPS consists of dividing the simulation box into three-dimensional equal-size subvolumes, where every subdomain gets assigned to one processor. In the SPARTIAN case, we combine different pair styles that result in an imbalance in computational load depending on whether particles are in the AT, HY or ideal gas regions. Hence, overall poor performance results from an increase in computational cost due to a uniform assignment of particles per processor.

To overcome this limitation, we use the shift scheme as implemented in LAMMPS[4]. Here, we assign a weight factor that tends to balance the computational load of each processor. A weight factor (>1) associated with a given particle determines how much more computational resources are devoted to this particle than the other particles present in the simulation. To illustrate this point, we consider SPC/E water in a simulation box of size 150 Å, running on (i) 200, (ii) 800 and (iii)
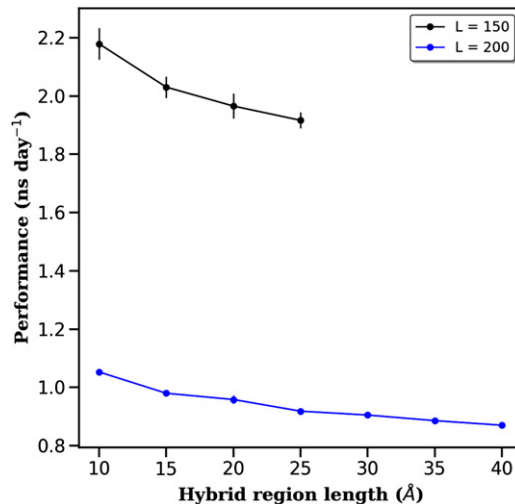
1200 processors. By using a weight factor of ten between the particles in the AT and HY regions and the particles in the IG region, we obtain an increase in performance of (i) 60%, (ii) 47% and (iii) 24%, respectively.

These results are encouraging, however, a more important advancement, from both fundamental and technical perspectives, is related to the implementation of particle-insertion methods that allows us to significantly reduce the size of the IG region while effectively including an infinite size reservoir [12].

3.4. Binary mixtures: extremely diluted conditions

The accuracy of the calculation of the excess chemical potential in the SPARTIAN method improves upon increasing the number of molecules present in the HY region, as it is apparent from equation (18). Thus, we expect that the SPARTIAN calculation requires a major increase in HY region size to converge μ^{exc} for low-density liquids and highly-diluted mixtures. To investigate these conditions, we simulate A-B LJ mixtures with $x_A = 0.1$ the mole fraction of A-molecules. In this case, we use a tetragonal simulation box, $L_x \times L_y \times L_z$ with its major axis, L_x, aligned along the *x*-direction (figure 6). The switching field $\lambda(x)$ is applied only along L_x and, in all cases considered, we keep constant the length of the AT, HY and IG regions. We also keep constant L_z. To increase the size of the system, and therefore the statistics for the SPARTIAN calculation, we start from $L_y = L_z$ and keep increasing L_y. To sum up, we have a simulation box with $L_x = 36\sigma$, $L_z = 5\sigma$ and variable L_y.

We simulate systems with 3.6, 10.8, 36, 54, 100, 250, 300, 500, 1000 and 1500 ($\times 10^3$) particles. The results are expressed in LJ reduced units. The force field parameters were chosen as $\sigma_{AA} = \sigma_{AB} = \sigma_{BB} = 1.0\sigma$, and $\epsilon_{AA} = \epsilon_{BB} = \epsilon_{AB} = 1.0\epsilon$, and the interactions were truncated to a cutoff radius equal to 2.5σ. The systems were equilibrated in the NPT ensemble with $T^* = 2.0 k_B \epsilon^{-1}$ and $P^* = 5.0 \sigma^3 \epsilon^{-1}$, by $1.0 \times 10^5 \tau$, using

---

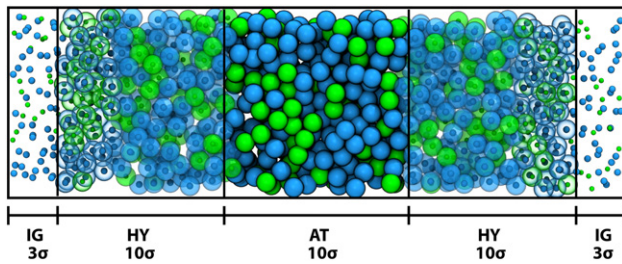[4] https://lammps.sandia.gov/doc/balance.html.

Figure 6. Lateral view of the tetragonal simulation setup used to investigate diluted LJ mixtures. The long axis of the box, where the adaptive resolution takes place, is aligned along the *x*-direction. The *y*-direction, with normal vector entering the page, is used to linearly increase the size of the system, thus increasing the number of particles (statistics) in the HY region.
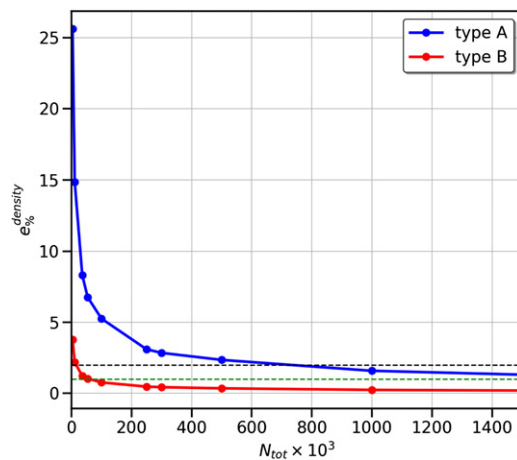

Figure 7. Error (deviation from target value) in the density as a function of total number of particles. $N_A = 0.1N_{tot}$. Black and green dashed lines correspond to 2% and 1% limits, respectively.

Nosé–Hoover thermostat and barostat with damping coefficient equal to $10\,\tau$ and $100\,\tau$, respectively and time step equal to $0.005\,\tau$. Then, the systems were simulated in the NVT ensemble with $T^* = 2.0 k_B \epsilon^{-1}$, by $1.0 \times 10^5 \tau$, using Langevin thermostat with damping parameter equal to $100\,\tau$ and time step equal to $0.001\,\tau$. In all cases, the SPARTIAN calculation were run with the AT region width and the HY region thickness equal to $10\,\sigma$ and $10\,\sigma$, respectively, as shown in figure 6. The drift and thermodynamic forces were calculated every $10\,\tau$.

One diagnostic tool to evaluate the quality of the SPARTIAN calculation is the density profile. Figure 7 shows the error, written as a relative difference from the target density, as a function of the number of particles in the LJ mixture. As expected, due the high concentration of B-particles ($0.9\,N_{tot}$), the deviation from the target value for this species is less than 2 %. This is the case for all the systems considered, except for the smallest system size (3600 particles). For the systems with larger number of particles, the error quickly decreases below 1%. However, for A-particles, the deviation from the target density only reaches the mark of 2% for systems composed of more than one million particles. It does not reach the 1% limit even for the system with 1.5 million particles.
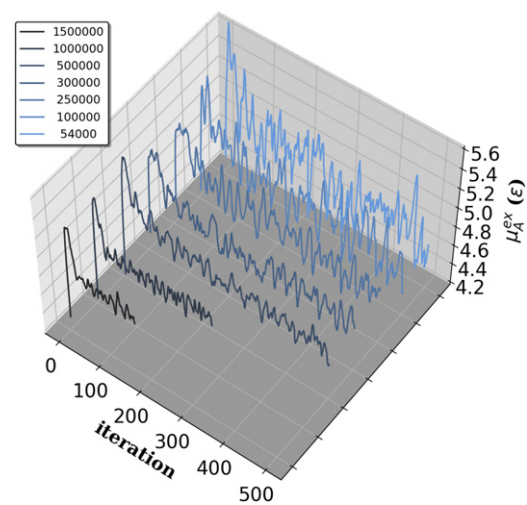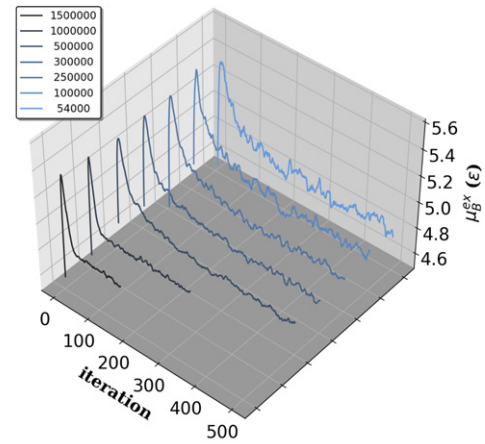

Figure 8. (top) Excess chemical potential convergence for B-particles. $N_B = 0.9N_{tot}$. (bottom) Excess chemical potential convergence for A-particles. $N_A = 0.1N_{tot}$.

Figure 8 shows the influence of the density in the calculation of the excess chemical potential using SPARTIAN. Figure 8(top) displays the excess chemical potential of B-particles, μ_B^{exc}, as a function of the total number of particles in the system. It is apparent that μ_B^{exc} moderately fluctuates in the systems with small number of particles and that this fluctuation significantly decreases for larger systems. However, due to the low concentration of A-particles, and high deviation in their density profile with respect to the target density, the excess chemical potential, μ_A^{exc}, fluctuates more distinctly for systems with total number of particles $<250\,000$, as shown in figure 8(bottom). These results are summarised in table 2 where excess chemical potential values, averaged over the last twenty SPARTIAN iterations, are presented as a function of the system size. Table 3 and figure 9 show the relative error $\sigma^\%(\mu_i^{exc})$ in the excess chemical potential for particles of type A and B, calculated over the last twenty SPARTIAN iterations. The value of the relative error for B-particles, $\sigma^\%(\mu_B^{exc})$, is less than 1.0% for all systems considered (except for the smallest number of particles-3600). However, for A-particles, the value

Table 2. Excess chemical potential (and standard deviation) for the LJ mixture as a function of system size. The data was obtained using the last twenty SPARTIAN iterations.

| N_{tot} | $\mu_{\text{exc}}(\epsilon)$ | |
	A	B
3600	5.186 ± 0.671	5.100 ± 0.092
54 000	4.567 ± 0.148	4.757 ± 0.021
100 000	4.661 ± 0.147	4.746 ± 0.024
250 000	4.718 ± 0.034	4.731 ± 0.010
300 000	4.718 ± 0.098	4.715 ± 0.015
500 000	4.653 ± 0.075	4.727 ± 0.008
1000 000	4.782 ± 0.033	4.769 ± 0.004
1500 000	4.777 ± 0.045	4.780 ± 0.005

Table 3. Relative error in the excess chemical potential for LJ mixture[a]

| N_{tot} | $\sigma^{\%}(\mu_i^{\text{exc}})$ | |
	A	B
3600	12.9476	1.8074
54 000	3.2379	0.4346
100 000	3.1607	0.5141
250 000	0.7209	0.2039
300 000	2.0773	0.3241
500 000	1.6033	0.1610
1000 000	0.6850	0.0790
1500 000	0.9340	0.1020

[a]Relative standard deviation for the last twenty iterations.
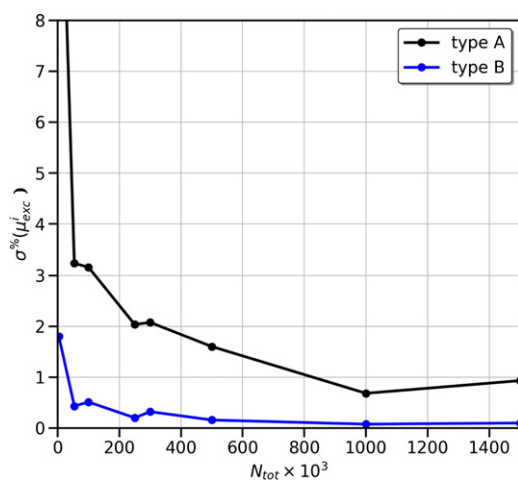
Figure 9. Relative error in the excess chemical potential, calculated over the last twenty iterations, as a function of total number of particles. $N_{\text{A}} = 0.1 N_{\text{tot}}$ and $N_{\text{B}} = 0.9 N_{\text{tot}}$.

of $\sigma^{\%}(\mu_{\text{A}}^{\text{exc}})$ only falls above 1.0% for systems with size equal or larger than one million particles, reaching the limit of 2.0% for systems with $N_{\text{tot}} > 300\,000$ particles.

3.5. Binary mixtures: SPARTIAN and KB analysis

The final example corresponds to the calculation of the excess chemical potential for a more realistic binary
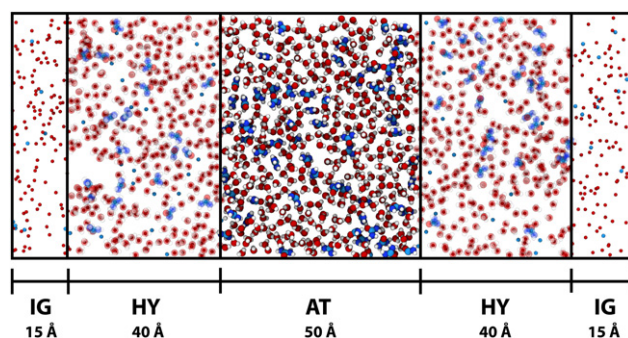
Figure 10. Lateral view of a slice of the tetragonal simulation setup used to investigate aqueous urea solutions. The long axis of the box, where we apply the adaptive resolution, is aligned along the *x*-direction. The linear size in the *y*-direction is 62.0 Å (the slice's thickness is 5.0 Å).
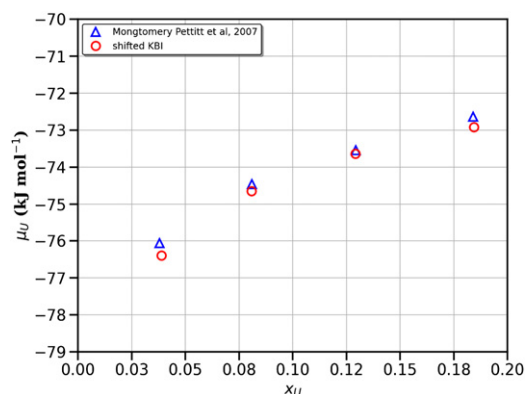
Figure 11. Chemical potential of urea in aqueous solution as a function of urea mole fraction.

mixture. In this case, we consider aqueous urea solutions [28–30]. We expect that, when increasing the system's complexity, SPARTIAN becomes a robust alternative to existing computational methods.

An initial configuration having 14500 SPC/E [25–27] water molecules and 2147 urea molecules [28] representing an aqueous urea solution at 0.1292 mole fraction (6M) is generated and optimised by adjusting the *y*-direction of the simulation cell. The size of the resulting simulation box is $160 \times 62 \times 60$ Å^3. To equilibrate the system, we performed fully AT simulations in the NPT ensemble for 20 ns at 298.0 K at 1.0 bar pressure using Nosé–Hoover thermostat and barostat with damping coefficients 100 fs and 1000 fs, respectively. This step is followed by 10 ns simulation in the NVT ensemble using Langevin thermostat with a damping coefficient of 100 fs. The SPARTIAN setup is presented in figure 10. Every iteration takes 20 ps to be completed.

We also performed fully-atomistic simulations at different urea mole fractions: 0.0389 (2M), 0.0809 (4M), 0.1292 (6M) and 0.1844 (8M) and carried out a KB analysis [40, 41] to compute the shifted urea chemical potential as a function of solute concentration. We use the SPARTIAN calculation at 6M as a reference value for the KB analysis. Results are presented in figure 11 where a comparison with absolute values reported in the literature [42] is also included. Our results indicate that

the combination of the KB-based method to obtain the trend with concentration, together with a more refined method like `SPARTIAN` to compute the reference value of the chemical potential, constitutes a useful tool for the calculation of free energy differences in complex molecular fluids and mixtures.

4. Concluding remarks

In the H–AdResS method [6, 7], the simulation of coexisting AT and ideal gas representations of a physical system is made possible by introducing a switching field that modulates the intermolecular potential. By including in the Hamiltonian an external potential, functional of the switching field, we build a grand potential for an inhomogeneous system. With this grand potential at hand, we find a parallel with DFT. Thus, we show that the external potential that balances the density across the simulation box is the excess chemical potential of the AT system [9]. Due to DFT's one-to-one correspondence between the density and the external potential, the use of one-body forces to impose a constant density profile, whose integral automatically gives the system's excess chemical potential, is compatible with a Hamiltonian description of the system. The resemblance with thermodynamic integration is apparent. Therefore, we dubbed the method `SPARTIAN` (spatially-resolved thermodynamic integration) [9].

We then use the `SPARTIAN` method to compute μ^{exc} for water, aqueous urea solutions and LJ mixtures. Our results well compare with values reported in the literature, when available. We verify that upon increasing the size of the HY region, which improves the statistics while keeping constant the AT region's size, μ^{exc} consistently converges with a modest decrease in computing efficiency. Our results also show an excess computational overhead when compared to fully AT simulations. This overhead is mainly due to domain decomposition and communication issues that result from an inefficient assignment of processors in the IG region. A preliminary experiment shows that `SPARTIAN` efficiently improves with a moderate fine-tuning effort aiming at optimising domain decomposition features. Nevertheless, the computation of chemical potentials is efficient and accurate. For water and aqueous urea solutions, we get a well-converged result after a few `SPARTIAN` iterations that correspond to simulate the system for just a couple of ns. Furthermore, size constraints are not an issue in `SPARTIAN` thanks to the particle-insertion method that we have recently developed, implemented and validated [12]. We also consider highly-diluted conditions in which we expect the `SPARTIAN` method to underperform compared to state-of-the-art computational methods. Still, our results display a convincing convergence of the excess chemical potential for all species involved in the system under such conditions. However, this requires a substantial increase in the system size. Hence, depending on the system's complexity, the choice of a computational method becomes a trade-off between efficiency, user-friendliness and accuracy. In particular, standard thermodynamic integration or particle-insertion-based methods applied to molecular mixtures require a careful design of an alchemical path. In the `SPARTIAN` case, once we obtain the initial configuration (following standard molecular dynamics)

and decide the parameters, the simulation automatically finds μ^{exc}. Indeed, depending on the problem at hand, a combination of methods might result advantageous. In case of investigating a solution's phase diagram, where it is necessary to compute μ^{exc} as a function of the solute's concentration, we propose to combine a KB theory approach with only one `SPARTIAN` calculation at a given (preferably high) concentration.

Finally, the thermodynamically consistent coupling of AT and ideal representations opens various interesting research avenues [43]. A straightforward application concerns the calculation of free energy differences [44]. Moreover, non-equilibrium conditions [45] can be readily imposed on the ideal gas reservoir and investigated on the AT region [12]. Finally, this and similar ideas originated from the adaptive resolution method could also be incorporated into QM/MM approaches [46, 47].

ORCID iDs

L A Baptista https://orcid.org/0000-0002-1419-6070
R C Dutta https://orcid.org/0000-0003-4068-2723
M Sevilla https://orcid.org/0000-0002-2197-1637
M Heidari https://orcid.org/0000-0002-8081-6602
R Potestio https://orcid.org/0000-0001-6408-9380
K Kremer https://orcid.org/0000-0003-1842-9369
R Cortes-Huerto https://orcid.org/0000-0002-4318-970X

References

[1] Praprotnik M, Delle Site L and Kremer K 2005 Adaptive resolution molecular-dynamics simulation: changing the degrees of freedom on the fly *J. Chem. Phys.* **123** 224106–14
[2] Praprotnik M, Delle Site L and Kremer K 2006 Adaptive resolution scheme for efficient hybrid atomistic-mesoscale molecular dynamics simulations of dense liquids *Phys. Rev.* E **73** 066701
[3] Praprotnik M, Delle Site L and Kremer K 2007 A macromolecule in a solvent: adaptive resolution molecular dynamics simulation *J. Chem. Phys.* **126** 134902
[4] Praprotnik M, Site L D and Kremer K 2008 Multiscale simulation of soft matter: from scale bridging to adaptive resolution *Annu. Rev. Phys. Chem.* **59** 545–71
[5] Fritsch S, Junghans C and Kremer K 2012 Structure formation of toluene around c60: implementation of the adaptive resolution scheme (address) into gromacs *J. Chem. Theory Comput.* **8** 398–403

[6] Potestio R, Fritsch S, Español P, Delgado-Buscalioni R, Kremer K, Everaers R and Donadio D 2013 Hamiltonian adaptive resolution simulation for molecular liquids *Phys. Rev. Lett.* **110** 108301

[7] Potestio R, Español P, Delgado-Buscalioni R, Everaers R, Kremer K and Donadio D 2013 Monte Carlo adaptive resolution simulation of multicomponent molecular liquids *Phys. Rev. Lett.* **111** 060601

[8] Kreis K, Fogarty A C, Kremer K and Potestio R 2015 Advantages and challenges in coupling an ideal gas to atomistic models in adaptive resolution simulations *Eur. Phys. J. Spec. Top.* **224** 2289–304

[9] Heidari M, Kremer K, Cortes-Huerto R and Potestio R 2018 Spatially resolved thermodynamic integration: an efficient method to compute chemical potentials of dense fluids *J. Chem. Theory Comput.* **14** 3409–17

[10] Español P, Delgado-Buscalioni R, Everaers R, Potestio R, Donadio D and Kremer K 2015 Statistical mechanics of Hamiltonian adaptive resolution simulations *J. Chem. Phys.* **142** 064115

[11] Nathan A and Guy M 2000 Density functional theory: an introduction *Am. J. Phys.* **68** 69–79

[12] Heidari M, Kremer K, Golestanian R, Potestio R and Cortes-Huerto R 2020 Open-boundary Hamiltonian adaptive resolution. from grand canonical to non-equilibrium molecular dynamics simulations *J. Chem. Phys.* **152** 194104

[13] Delgado-Buscalioni R, Kremer K and Praprotnik M 2008 Concurrent triple-scale simulation of molecular liquids *J. Chem. Phys.* **128** 114110

[14] Fritsch S, Poblete S, Junghans C, Ciccotti G, Delle Site L and Kremer K Apr 2012 Adaptive resolution molecular dynamics simulation through coupling to an internal particle reservoir *Phys. Rev. Lett.* **108** 170602

[15] Mukherji D and Kremer K 2013 Coil-globule-coil transition of PNIPAm in aqueous methanol: coupling all-atom simulations to semi-grand canonical coarse-grained reservoir *Macromolecules* **46** 9158–63

[16] Wang H, Hartmann C, Schütte C and Delle Site L 2013 Grand-canonical-like molecular-dynamics simulations by using an adaptive-resolution technique *Phys. Rev. X* **3** 011018

[17] Agarwal A, Zhu J, Hartmann C, Wang H and Site L D 2015 Molecular dynamics in a grand ensemble: Bergmann-Lebowitz model and adaptive resolution simulation *New J. Phys.* **17** 083042

[18] Delle Site L, Krekeler C, Whittaker J, Agarwal A, Klein R and Höfling F 2019 Molecular dynamics of open systems: construction of a mean-field particle reservoir *Adv. Theory Simul.* **2** 1900014

[19] Roth R 2006 *Introduction to density functional theory of classical systems: theory and applications* https://tat.physik.uni-tuebingen.de/~kley/lehre/cp-prakt/projekte/3_lattice-dft-oettel.pdf

[20] Oettel M 2018 *Classical density functional theory: exact density distribution of hard rods between walls in 1D* https://bytebucket.org/knepley/cdft-git/wiki/papers/Lecture_Notes_on_DFT__Roland_Roth.pdf?rev=824276d909d430b7105ca482b6daac52333a4579

[21] Kirkwood J G 1935 Statistical mechanics of fluid mixtures *J. Chem. Phys.* **3** 300–13

[22] Mermin N D 1965 Thermal properties of the inhomogeneous electron gas *Phys. Rev.* **137** A1441–3

[23] Dünweg B 1993 Molecular dynamics algorithms and hydrodynamic screening *J. Chem. Phys.* **99** 6977–82

[24] Heidari M, Cortes-Huerto R, Donadio D and Potestio R 2016 Accurate and general treatment of electrostatic interaction in Hamiltonian adaptive resolution simulations *Eur. Phys. J. Spec. Top.* **225** 1505–26

[25] Berendsen H J C, Grigera J R and Straatsma T P 1987 The missing term in effective pair potentials *J. Phys. Chem.* **91** 6269–71

[26] Dang L X and Pettitt B M 1987 Simple intramolecular model potentials for water *J. Phys. Chem.* **91** 3349–54

[27] Wu Y, Tepper H L and Voth G A 2006 Flexible simple point-charge water model with improved liquid-state properties *J. Chem. Phys.* **124** 024503

[28] Weerasinghe S and Smith P E 2003 A Kirkwood−Buff derived force field for mixtures of urea and water *J. Phys. Chem.* B **107** 3891–8

[29] Mukherji D, van der Vegt N F A, Kremer K and Kremer K 2012 Preferential solvation of triglycine in aqueous urea: an open boundary simulation approach *J. Chem. Theory Comput.* **8** 3536–41

[30] de Oliveirade Oliveira T E, Netz P A, Kremer K, Junghans C and Mukherji D 2016 C-IBI: targeting cumulative coordination within an iterative protocol to derive coarse-grained models of (multi-component) complex fluids *J. Chem. Phys.* **144** 174106

[31] Plimpton S 1995 Fast parallel algorithms for short-range molecular dynamics *J. Comput. Phys.* **117** 1–19

[32] Wolf D, Keblinski P, Phillpot S R and Eggebrecht J 1999 Exact method for the simulation of Coulombic systems by spherically truncated, pairwise 1/r summation *J. Chem. Phys.* **110** 8254–82

[33] Zahn D, Schilling B and Kast S M 2002 Enhancement of the wolf damped coulomb potential: static, dynamic, and dielectric properties of liquid water from molecular simulation *J. Phys. Chem.* B **106** 10725–32

[34] Fanourgakis G S 2015 An extension of wolf's method for the treatment of electrostatic interactions: application to liquid water and aqueous solutions *J. Phys. Chem.* B **119** 1974–85

[35] Fennell C J and Daniel Gezelter J 2006 Is the ewald summation still necessary? pairwise alternatives to the accepted standard for long-range electrostatics *J. Chem. Phys.* **124**

[36] Ryckaert J-P, Ciccotti G and Berendsen H J C 1977 Numerical integration of the cartesian equations of motion of a system with constraints: molecular dynamics of n-alkanes *J. Comput. Phys.* **23** 327–41

[37] Ben-Naim A and Marcus Y 1984 Solvation thermodynamics of nonionic solutes *J. Chem. Phys.* **81** 2016–27

[38] Mester Z and Panagiotopoulos A Z 2015 Mean ionic activity coefficients in aqueous nacl solutions from molecular dynamics simulations *J. Chem. Phys.* **142** 044507

[39] Sauter J and Grafmüller A 2016 Predicting the chemical potential and osmotic pressure of polysaccharide solutions by molecular simulations *J. Chem. Theory Comput.* **12** 4375–84

[40] Cortes-Huerto R, Kremer K and Potestio R 2016 Communication: Kirkwood-buff integrals in the thermodynamic limit from small-sized molecular dynamics simulations *J. Chem. Phys.* **145** 141103

[41] Heidari M, Kremer K, Potestio R and Cortes-Huerto R 2018 Finite-size integral equations in the theory of liquids and the thermodynamic limit in computer simulations *Mol. Phys.* **116** 3301–10

[42] Kokubo H, Rösgen J, Bolen D W and Pettitt B M 2007 Molecular basis of the apparent near ideality of urea solutions *Biophys. J.* **93** 3392

[43] Qi S, Behringer H, Raasch T and Schmid F 2016 A hybrid particle-continuum resolution method and its application to a homopolymer solution *Eur. Phys. J. Spec. Top.* **225** 1527–49

[44] Heidari M, Cortes-Huerto R, Potestio R and Kremer K 2019 Steering a solute between coexisting solvation states: revisit-

ing nonequilibrium work relations and the calculation of free energy differences *J. Chem. Phys.* **151** 144105

[45] Stalter S, Yelash L, Emamy N, Statt A, Hanke M, Lukáčová-Medvid'ová M and Virnau P 2018 Molecular dynamics simulations in hybrid particle-continuum schemes: pitfalls and caveats *Comput. Phys. Commun.* **224** 198–208

[46] Boereboom J M, Potestio R, Donadio D and Bulo R E 2016 Toward Hamiltonian adaptive qm/mm: accurate solvent structures using many-body potentials *J. Chem. Theory Comput.* **12** 3441–8

[47] Delle Site L 2018 Simulation of many-electron systems that exchange matter with the environment *Adv. Theor. Simul.* **1** 1800056